Dy doped $SrTiO_3$: a promising anodic material in Solid Oxide Fuel Cells

Saurabh Singh[a], Prabhakar Singh[a], Massimo Viviani[b], Sabrina Presto[b,*]

[a] Department of Physics, Indian Institute of Technology (Banaras Hindu University), Varanasi-221005, India, saurabh.singhiitbhu@gmail.com (S. S.), psingh.app@iitbhu.ac.in (P. S.)

[b] CNR-ICMATE, c/o DICCA-UNIGE, Via all'Opera Pia 15, 16145, Genova, Italy, massimo.viviani@cnr.it (M. V.) sabrina.presto@cnr.it (S. P.)

[*] corresponding author; telephone: +3901064756025; fax: +3901064756028; sabrina.presto@cnr.it

Abstract

The perovskite-type oxides, having a general formula ABO_3, are promising candidates for anode materials in solid oxide fuel cells. In particular, doped $SrTiO_3$ based perovskites are potential mixed ionic-electronic conductors and they are known to have excellent thermal and chemical stability along with carbon and sulfur tolerance. In this work, $Dy_xSr_{1-x}TiO_{3-\delta}$ system with x = 0.03, 0.05, 0.08 and 0.10 is studied to understand the influence of Dy content on its structural and electrical behavior. Electrochemical properties are measured, both in air and hydrogen atmosphere, and structural characterizations are performed before and after electrochemical tests and compared each other to study the stability. Results show that $Dy_xSr_{1-x}TiO_{3-\delta}$ powders with $x \leq 0.05$, are single phase, while for $x \geq 0.08$ a small amount of secondary phases is formed. In air, the conductivity is predominantly mixed ionic-electronic type for $x \leq 0.05$, becoming ionic for $x \geq 0.08$. It is observed that conductivity, for each composition, increases passing from air to hydrogen and activation energy decreases. $Dy_{0.05}Sr_{0.95}TiO_{3-\delta}$ shows the highest conductivity in air whereas $Dy_{0.08}Sr_{0.92}TiO_{3-\delta}$ in H_2 atmosphere. Degradation observed by XRD is negligible for $x \leq 0.05$ but increases with higher Dy content.

Keywords: anode; conductivity; reduction; perovskite; hydrogen; phase stability.

1. Introduction.

The recent upsurge in global energy demand and global warming due to increasing carbon footprint have a detrimental effect on the environment which enforces to look for alternative models for energy production and management. Solid oxide fuel cells (SOFC) are highly efficient devices for energy production, converting chemical energy directly into electrical energy without involving the combustion process [1-4]. SOFC are being considered for commercial exploitation in stationary applications due to their high energy conversion efficiency and fuel flexibility [5, 6]. The challenges for the commercialization of SOFC are to reduce cost and increase the reliability of the system. Enormous effort in research is going in the direction of lowering the temperature of SOFC from 800 °C to less than 700 °C in order to reduce problems connected to high temperature [7-9], that means finding new materials with suitable electrocatalytic activity at that temperature. To improve performances of fuel cells there are different paths: the first is finding new designs of cells and stacks. Several designs of planar fuel cells are reported in literature: some very standard and now consolidated, that are anode or cathode supported [10] and metal-supported [11], some very innovative and still in development. Among them, the so called "Evolve cell" relies on a supporting current collector made of a ceramic - metal composite in the form of a metallic Ni-Cr-Al based foam, impregnated with conductive La-doped $SrTiO_3$-based ceramics. Its advantage is to provide the structural stability to the cell, but also to play the role of current collector due to the impregnation with a ceramic material [12]. Other innovative designs are: the Dual Membrane cell [13, 14], exploiting properties of a mixed anionic and protonic conductor used as central membrane, and electrolyte supported cells in symmetrical configuration [15]. Both designs appear to be useful as reversible solid oxide cells.

Another way is to study new materials to be used in the state of art architecture. In particular anode plays an important role as constituent part of SOFCs, where the fuel is oxidized and electrons are released to the external circuit.

Over the past few years, several materials have been investigated as anode materials for SOFC application [7]. Nowadays, Ni-YSZ based anode is widely used for SOFC, although facing long-term instability issues and suffering from carbon and sulfur poisoning and agglomeration of nickel particles at elevated temperature [16, 17]. Therefore, development of new alternative anode materials able to withstand redox cycling and hydrocarbon fuels is needed.

The perovskite-type oxides having a general formula ABO_3, are promising candidates for anode materials of solid oxide fuel cells. $SrTiO_3$ is a potential mixed ionic-electronic conductor for SOFC anode application which is known to have excellent thermal and chemical stability along with carbon and sulfur tolerance [18-22]. However, pure $SrTiO_3$ cannot be used as anode material due to its low electrical conductivity. Therefore, donor doped $SrTiO_3$ have been developed to enhance the electrical conductivity under reducing conditions [23]. Under reducing atmosphere, redox coupling (Ti^{4+}/Ti^{3+}) occurs in $SrTiO_3$ which exhibits n-type semiconducting behavior.

La–doped $SrTiO_3$ (LST) [24, 25] exhibits n-type semiconducting behavior when it is donor-doped and/or exposed to a reducing atmosphere. Lanthanum is a good donor dopant because the La^{3+} ionic radius (1.32 Å, coordination 12) is similar to that of Sr^{2+} (1.44 Å, coordination 12). Under oxidizing conditions, the compensation occurs through the formation of Sr vacancies in the lattice, coupled with the formation of SrO layers within the structure. Under reducing conditions, Sr vacancies and SrO layers are eliminated, and the charge compensation for La^{3+} ions becomes electronic through the formation of electrons in the conduction band, i.e. conversion of Ti^{4+} to Ti^{3+} [23].

A lot of elements as Cu, Ba, Ca, Mo, and Ta [26], and several rare earths, Ce [26], Y [26-30], Sm [31], Pr [32] were also tested as possible donor materials on A site. Papers, reporting B site doped $SrTiO_3$ and LST [26, 33-37], or A and B site co-doped LST are also presented in literature [26, 38-40]. The conductivity found in doped ST ranges from 1 to 500 Scm^{-1} under reducing atmosphere and at SOFC operating temperatures (650÷800 °C), with highest values found in LST and with huge variations among different works probably due to the used of different sintering protocols.

Although some papers report investigations on Dy-$SrTiO_3$ for application in energy storage systems [41, 42], it has not been tested as SOFC material until now.

The ionic radius of Dy^{3+} (1.23 Å, CN 12) is close to that of Sr^{2+} [43], indicating that incorporation of Dy^{3+} is sterically favored at Sr-site. Lattice defect structure must be modified to maintain electro-neutrality due to charge imbalance between Dy^{3+} and Sr^{2+} ions, for instance with formation of oxygen-rich planes improving the ionic conductivity of Dy-doped $SrTiO_3$ [23, 44, 45]. In addition, Liu a et al. [46] reported high electronic conductivity of reduced Dy-doped $SrTiO_3$, indicating that it can be considered as anodic material for SOFC.

In this paper, the influence of Dy content on the structural and electrical behavior of $SrTiO_3$ prepared by auto-combustion route was studied. Properties were measured both in air and hydrogen atmosphere and discussed in detail.

2. Experimental

2.1 Powders synthesis

$Dy_xSr_{1-x}TiO_{3-\delta}$ powders with x = 0.03, 0.05, 0.08 and 0.10, called DST3, DST5, DST8 and DST10, respectively, were synthesized *via* citrate-nitrate auto-combustion route. The starting materials, Dy_2O_3 (99.9%), SrO (99.5%), $C_{12}H_{28}O_4Ti$ (97%) and citric acid were taken in appropriate amounts.

Dy_2O_3 and SrO were dissolved in distilled water in presence of nitric acid to give dysprosium and strontium nitrate, respectively. Then, the two solutions were mixed together and citric acid was also added. Another homogeneous solution containing titanium iso-propoxide ($C_{12}H_{28}O_4Ti$) in ethylene glycol was prepared at 100 ºC, that successively was added to nitrates solution, under a pH maintained at 2 by adding ammonium solution. White precipitate of titanium hydroxide was formed which was dissolved by adding a few drops of nitric acid under pH value of 2. The transparent solution was slowly evaporated on a hot plate at temperature 250 °C under continuous stirring *via* magnetic stirrer. After a few hours, it was converted into a gel and then converted into light brownish color ash. The as-prepared powder was grounded by mortar and pestle. To remove the organic binders and nitrates, it was calcined in air at 1000 °C for 10 hours in alumina crucible.

The calcined powders were pelletized in 12 mm disk by a hydraulic press at 5 tons. Thereafter, pellets were sintered in air at 1200 °C for 12 hours with heating rate of 5 ºC min^{-1} and then cooled down to room temperature.

2.2 Characterizations

X-ray diffraction (XRD, Rigaku Miniflex II desktop) with Cu- Kα radiation (λ = 1.54098 Å) in 2θ range from 20° to 70° with a step size of Δ2θ = 0.02° was used to characterize the phase structure of as sintered and after reduction $Dy_xSr_{1-x}TiO_3$ samples at room temperature. The Rietveld Refinement (RR) was also carried out using FULLPROF Suite software package with Pseudo-Voigt wave function. Microstrain and crystallite size were calculated from XRD patterns by using Williamson-Hall model here reported [47]:

$$\beta cos\theta = 0.9\,\lambda/t + 4\varepsilon sin\theta \quad (1)$$

where t is average crystallite size, ε is microstrain, β is full width half maxima (FWHM) at Bragg's angle (2θ) and λ being the X-ray wavelength of Cu-Kα. The relative density of each pellet was

measured by the Archimedes principle, employing Denver SI-234 density measurement kit. Microstructure of the samples was studied by field emission scanning electron microscope (FESEM, NOVA NANOSEM 450) and average grains size was statistically calculated by ImageJ software from the images. For electrical measurements, the sintered pellets were polished, coated with Ag-paste on both sides, and, finally, cured at 750 °C for 20 minutes. Electrical conductivity was measured in air between room temperature and 700 °C. Samples were then reduced at 700 °C for 24 h under pure flowing hydrogen and electrical conductivity was measured again down to room temperature. A four-probe test (Probostat, Norecs) was employed and impedance was measured by Frequency Response Analyzer and Potentiostat (IVIUMSTAT, Ivium Technologies), in the range of frequency between 10^0 – 10^6 Hz (10 points/decade).

3. Results and discussions

X-ray diffraction patterns of samples DST3-DST10, sintered in air, are shown in Figure 1, within the results of Rietveld refinement. All samples show cubic phase with space group $Pm\bar{3}m$ (ICDD Card Number: 86-0178). No impurity peaks were detected for the samples with $x \leq 0.05$, while traces of secondary phases were observed in the samples with $x \geq 0.08$. In particular, TiO_2 (ICDD Card Number: 21-1276) and Dy_2O_3 (ICDD Card Number: 01-078-0388) in DST8, while TiO_2 and pyrochlore $Dy_2Ti_2O_7$ (ICDD Card Number: 17-0453) were observed in DST10. The lattice parameters, and some reliability factors of RR are summarized in Table 1. From this table, it is observed that, lattice parameter decreases with increase in Dy content, which may be attributed to the replacement of the larger sized Sr^{2+} ions at A-sites of the perovskite structure by the smaller Dy^{3+} ions. Moreover, in all the refinements, the reliability factors are satisfactory, indicating a good refined crystal structure model representative of the real case. In case of DST8 and DST10, RR was performed also considering the secondary phases, and their amounts were evaluated as 3.5 wt.% of TiO_2 and 3 wt.% of Dy_2O_3 in DST8, 3 wt.% of TiO_2 and 2.4 wt.% $Dy_2Ti_2O_7$ in DST10.

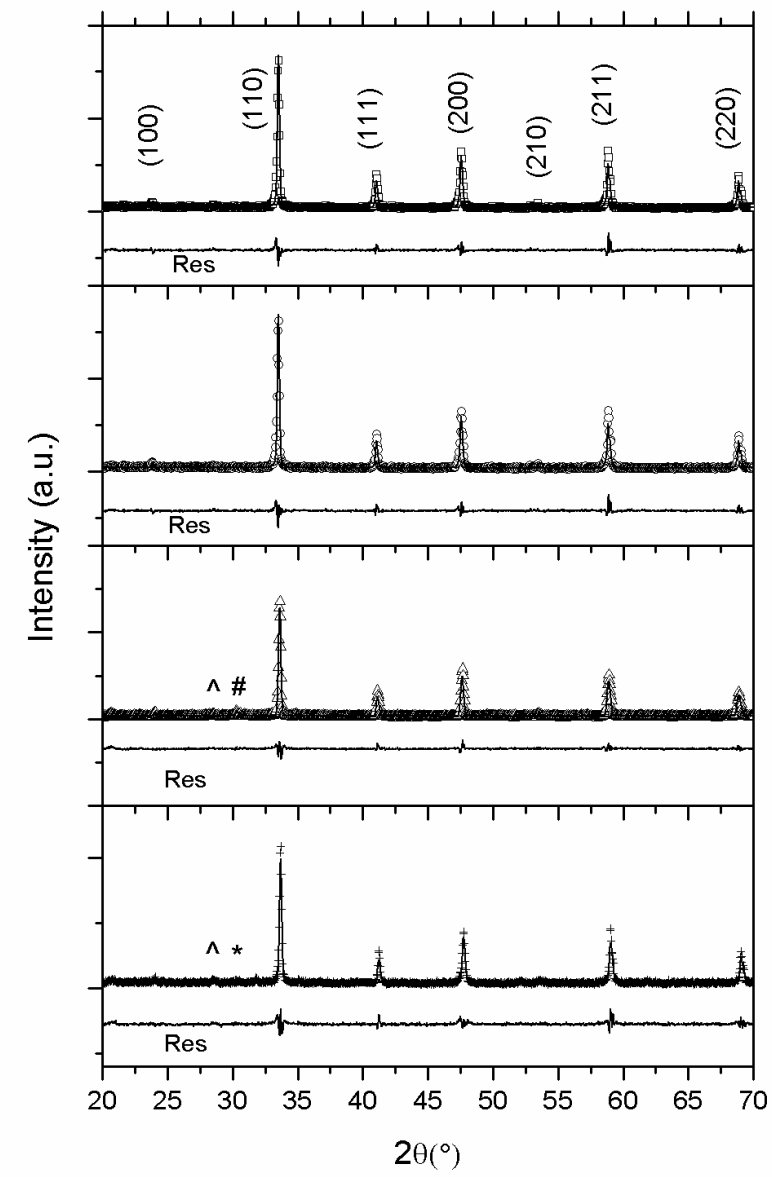

Figure 1. Rietveld refinement (-) of XRD patterns (□=DST3, ○=DST5, △= DST8 and +=DST10). Residuals (Res) and Miller indexes are also reported with major reflections of TiO_2 (^), Dy_2O_3 (#) and $Dy_2Ti_2O_7$ (*) secondary phases.

In Figure 2, the microstrain and crystallite size of the studied compositions are reported. Both variables show the same trend, being the minimum value of microstrain and crystallite size observed for the sample DST8.

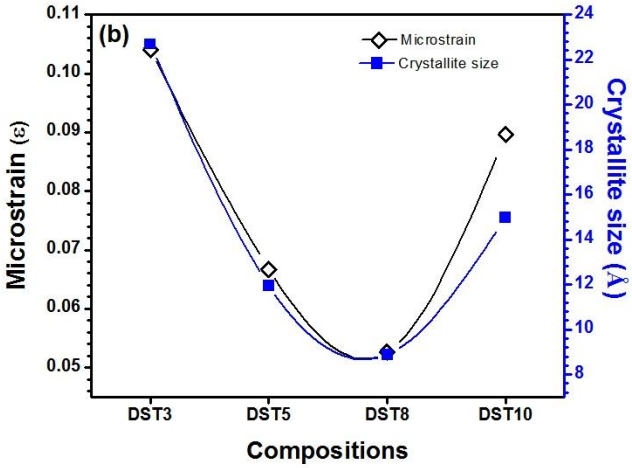

Figure 2. The calculated microstrain and crystallite size as function of Dy amount.

DST8 showed also the minimum of relative density, as reported in Table 1, that was confirmed by comparison of FESEM micrographs of fractured samples sintered at 1200 °C in air (Figure 3). The average grain size was also determined using ImageJ software, and was found to be 4.54 µm, 1.62 µm, 1.06 µm and 5.13 µm for DST3, DST5, DST8 and DST10, respectively. This trend can be considered as an effect of dopant segregation at the grain boundary, which inhibits the grain growth during sintering. In fact, segregation is known to be driven by the decrease in interfacial free energy that accompanies the densification process and is therefore a general feature of polycrystalline ceramics [48]. When dopant segregates in the pyrochlore secondary phase, that is the case of DST10, this effect is not present anymore; on the contrary this secondary phase can promote the increasing of grain size and densification [49].

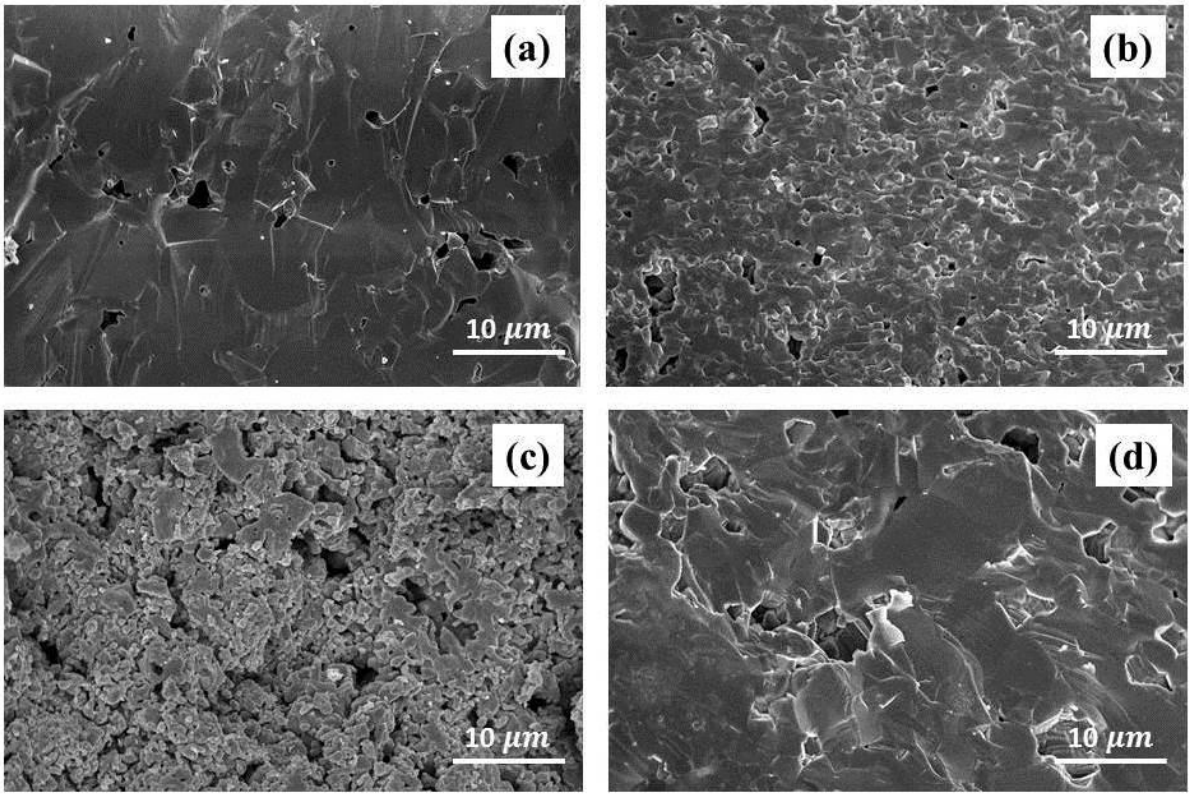

Figure 3. The FESEM micrographs of fractured compositions (a) DST3, (b) DST5, (c) DST8 and (d) DST10

Table 1: Rietveld refined parameters and relative density of studied compositions.

Sample	Lattice Parameter (Å)	$\chi 2$	R_B	R_F	Relative density (%)
DST3	3.91078	6.464	5.31	3.71	97.7
DST5	3.90996	6.19	4.75	3.75	95.7
DST8	3.90906	5.75	4.83	3.74	66.4
DST10	3.90823	6.68	5.29	4.03	87.9

Impedance measurements of all compositions were collected in air and hydrogen, at different temperatures. As an example, Nyquist plots of imaginary (Z'') vs. real (Z') impedance of sample DST3, measured in air at different temperatures, are reported in Figure 4. As it can be seen from such curves the contributions from grain boundaries and grain cores are not resolved and just one depressed semi-circle was observed in all cases, that was fitted by an equivalent circuit consisting of one parallel R-CPE element (R//Q) in series to a resistance R_0 simulating contact resistance, the latter due to weak variation with temperature of the mechanical load in the measurement rig.

After reduction, electronic conductivity measured in hydrogen increased significantly; under this circumstance, imaginary part of impedance was negligible and given by inductance of the measurement system, as demonstrated by impedance spectra collected on sample DST10 and shown in Fig. 5. Therefore, for reduced samples, R was obtained for each composition and temperature from the real part of impedance only.

The fitted R values were utilized to calculate the conductivity σ_p by the following equation:

$$\sigma_p = L/RA \quad (2)$$

where L is the thickness and A is the cross section area of specimens.

Conductivity was also corrected for porosity by following the Bruggeman Asymmetric Model [50, 51]. The model treats a continuous phase of conductivity σ_1 with an embedded discontinuous phase σ_2 and a volume fraction x_2:

$$(\sigma_1/\sigma_m) \cdot (\sigma_m - \sigma_2/\sigma_1 - \sigma_2)^3 = (1 - x_2)^3 \quad (3)$$

where σ_m is the conductivity of dispersion. In this case, x_2 is the porosity x_p, (as calculated from density reported in Table 1) and then σ_2=0 as the phase 2 corresponds to pores; σ_1= σ is the true conductivity of dense Dy-doped $SrTiO_3$, and σ_m is σ_p, the measured effective conductivity of porous pellet. In this hypothesis, eq. (3) can be written as:

$$\sigma = \sigma_p/\left(1 - x_p\right)^{3/2} \quad (4)$$

In Table 2, corrected conductivity values, σ, obtained in air and in hydrogen at 650°C, a standard operative temperature for a SOFC, are reported as a function of Dy content. Moreover, Arrhenius plots of conductivity in air and hydrogen, obtained for all compositions, are presented in Figure 6 and the activation energy (Ea), for conduction mechanism in air and hydrogen, was also reported in Table 2 as calculated from fitting of conductivity data to the Arrhenius equation:

$$\sigma \cdot T = A\exp\left(-E_a/kT\right) \quad (5)$$

Table 2: Conductivity values (σ) measured at 650°C and calculated energy activations (E_a) of conduction mechanism, for all composition, respectively in air and in hydrogen.

Sample	σ (650°C, O_2) 10^{-2}*Scm^{-1}	σ (650°C, H_2) 10^{-2}* Scm^{-1}	E_a (O_2) eV	E_a (H) eV
DST3	7.16 10^{-1}	3.125	0.77	0.17
DST5	9.88 10^{-1}	3.054	0.66	0.21
DST8	2 10^{-3}	13.639	1.42	0.10
DST10	4.4 10^{-2}	1.221	1.26	0.24

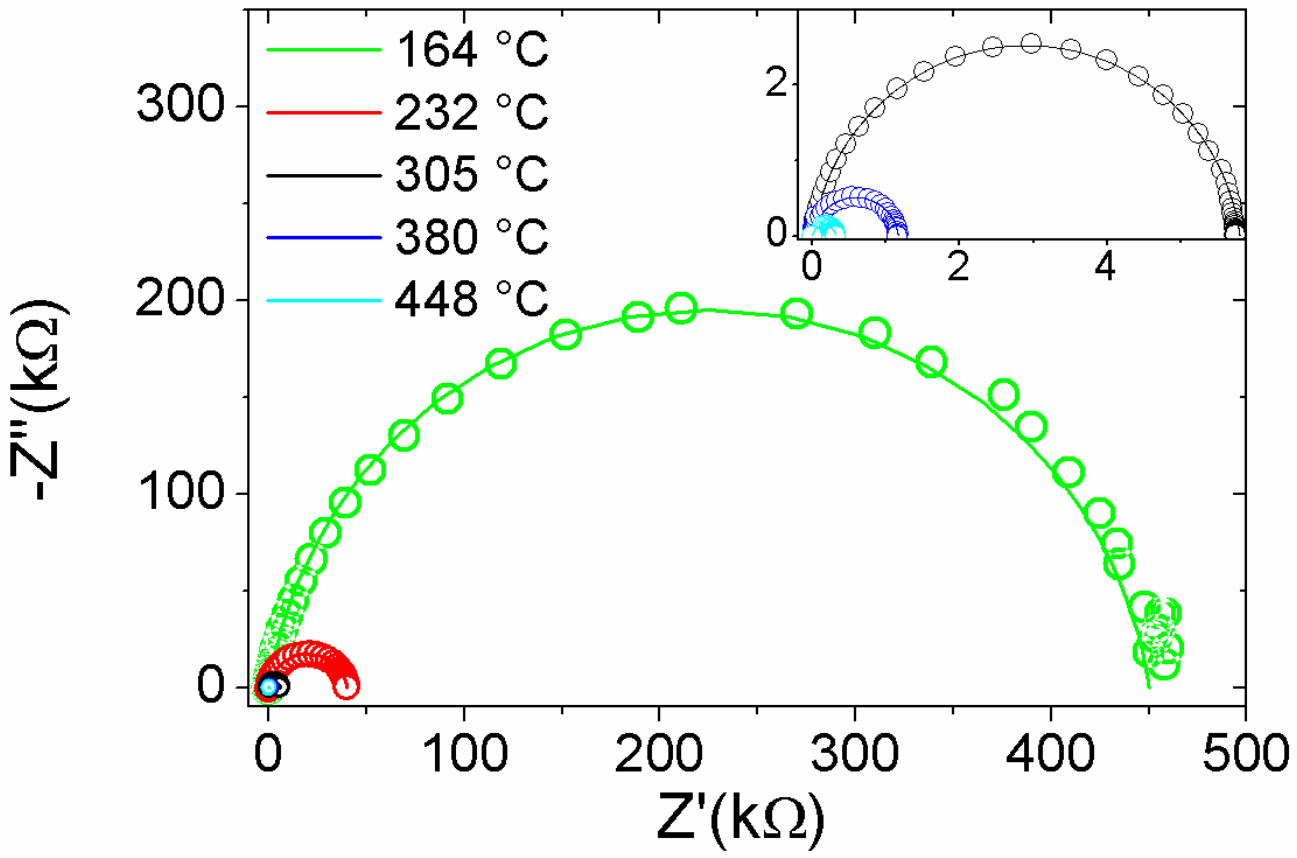

Figure 4. Nyquist plot of impedances measured in air for DST3 sample, at several temperatures as reported in the legend. The solid line was obtained by fitting the data with the equivalent circuit mentioned in the text.

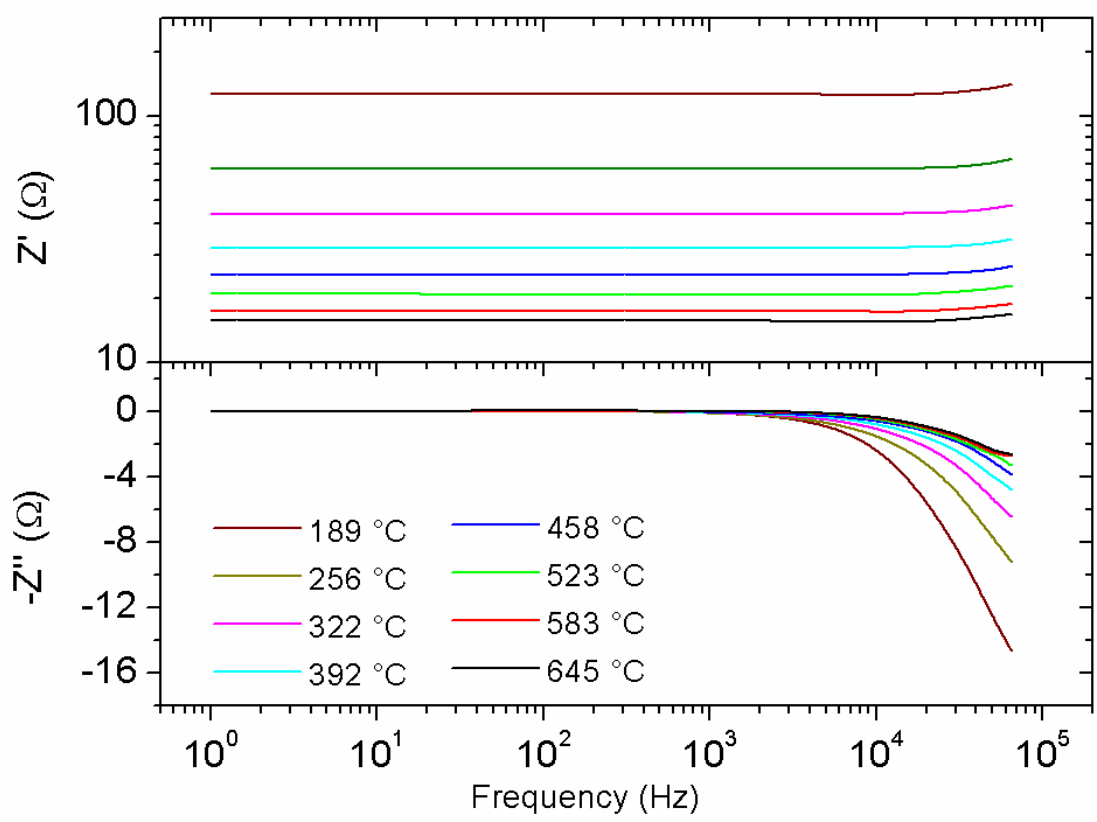

Figure 5. Impedance spectra of DST10 sample, measured in H_2, at several temperatures as reported.

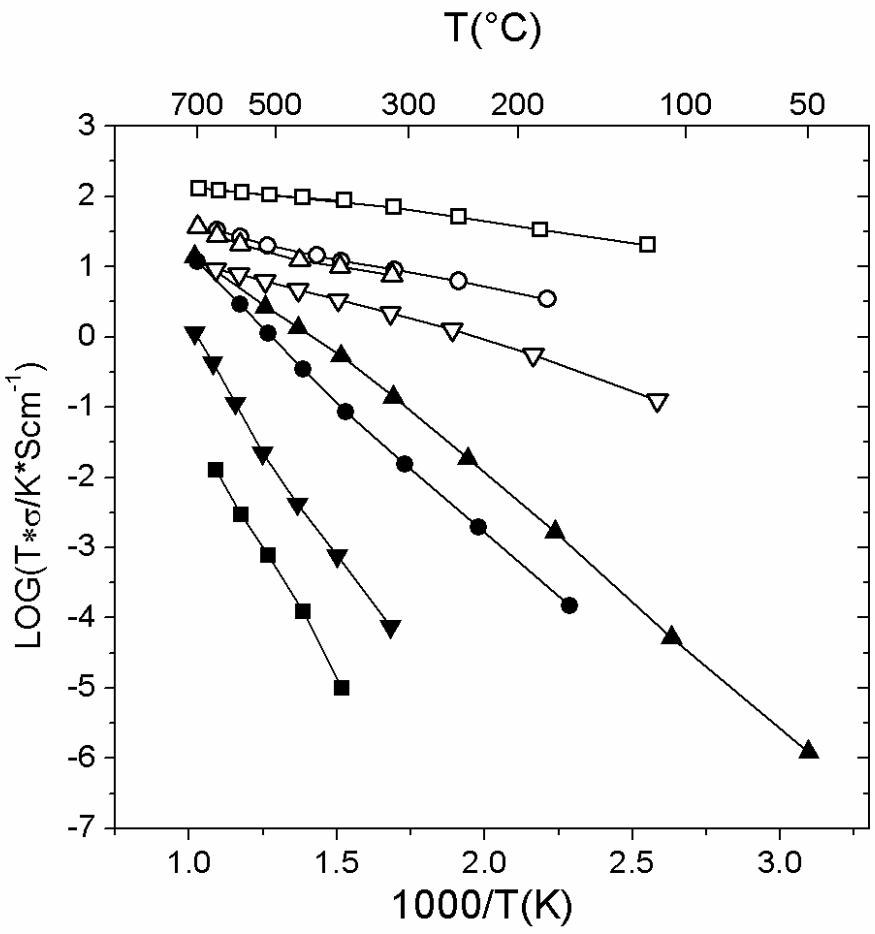

Figure 6. Arrhenius plot of conductivity of DST3 (●), DST5 (▲), DST8 (■) and DST10 (▼), samples as function of temperature, in air (full symbols) and in hydrogen (empty symbols). Lines are the best fit of Eq. (5) to experimental data.

It is observed that conductivity, for all compositions, increases passing from air to hydrogen. DST5 showed the highest conductivity in air whereas DST8 in H_2 atmosphere.

The activation energy calculated for all compositions is listed in Table 2. As the value of Ea is typically close to 1 eV for oxide ion conduction and to 0.1 eV for electronic conduction, with intermediate values for mixed conduction regimes [52, 53], data reported in Table 2 suggest mixed ionic-electronic

conduction for DST3 and DST5, differently from DST8 and DST10 where pure ionic conduction is likely to take place.

After reduction with H_2 the activation energy is further lowered, being in the range of 0.1 − 0.24 eV for all samples.

Above reported experimental observations can be explained by considering the incorporation mechanisms of dopant into the perovskite structure of $SrTiO_3$. Given the average value of ionic radius of Dy^{3+} in 6-fold coordination (0.91 Å) and in 12-fold coordination (1.23 Å) [43], three types of incorporation can be considered and expressed by the following equations written with the Kröger-Vink notation:

$$Dy_2O_3 + 2TiO_2 \xrightarrow{SrTiO_3} 2Dy_{Sr}^{\cdot} + 2Ti_{Ti}' + 6O_O^X + 1/2\, O_2 \quad (6a)$$

$$Dy_2O_3 \xrightarrow{SrTiO_3} Dy_{Sr}^{\cdot} + Dy_{Ti}' + 3O_O^X \quad (6b)$$

$$Dy_2O_3 \xrightarrow{TiO_2} 2Dy_{Ti}' + V_O^{\cdot\cdot} + 3O_O^X \quad (6c)$$

Eq. (6a) accounts for the incorporation at the Sr-site, with formation of positively charged defects, compensated by electrons or, equivalently, by partial reduction of Ti^{4+} to Ti^{3+}.

In the second case, eq. 6(b), the incorporation takes place both at Sr- and Ti-sites, with self-compensation of charges. Finally, eq. (6c) is relevant to the case of incorporation at the Ti-site with formation of negatively charged defects, compensated by oxygen vacancies.

As already reported in case of $BaTiO_3$, [54], the most energetically favorable incorporation mechanism for Dy^{3+} and similar rare-earths like Y, Er and Gd, is the self-compensation. However, other factors can determine the actual incorporation mechanism, the most important being the amount of dopant, the cationic ratio and the temperature.

Lattice parameters and strain are determined by the incorporation mechanism so that, minimal local distortion (microstrain) can be expected when Dy^{3+} is replacing both (larger) Sr^{2+} and (smaller, being its ionic radius in 6-fold coordination equal to 0.61 Å) Ti^{4+} atoms. The formation of the pyrochlore phase also introduces point defects, namely Ti vacancies, which affect the lattice size and strain state.

Moreover, results indicate that there is a regime change for $x \geq 0.08$, passing from a conductivity substantially mixed ionic-electronic type ($x \leq 0.05$) to a one ionic type ($x \geq 0.08$) with a significant decreasing of conductivity value (≈ 2 orders of magnitude at 650°C). In both the two regimes, the conductivity increases when increasing Dy content.

Therefore, for DST8 self-compensation (eq. 6b) is mainly active, which also reflect in lower conductivity and higher Ea, and causing the smaller microstrain and negligible amount of electrons, being the conduction of ionic nature and due to oxygen vacancies produced either intrinsically (Schottky disorder) or partially through mechanism of eq. (6c). Mechanism of eq. (6c) is more active in sample DST10, as demonstrated by higher conductivity, lower Ea and higher microstrain. In these samples, however, the presence of a secondary phase, i.e. of Ti vacancies in the main phase, may account for observed lowering of the unit cell volume.

Conversely, in case of DST3 and DST5, both the (6a) and (6b) eq. take place, giving higher microstrain, higher conductivity and lower Ea (ionic-electronic).

Under reducing atmosphere, lattice oxygen may be lost and thus oxygen vacancies will be generated,

$$2TiO_2 \rightarrow 2Ti'_{Ti} + V_O^{\cdot\cdot} + 3O_O^X + 1/2\, O_2 \quad (7)$$

In order to preserve the electro-neutrality, the following equation must be satisfied.

$$[Ti'_{Ti}] = [Dy^{\cdot}_{Sr}] + 2[V_O^{\cdot\cdot}] \quad (8)$$

Therefore, both extrinsic defects introduced by Dy incorporation at Sr-site and intrinsic oxygen vacancies, which are formed under reducing conditions, contribute to the formation of electrons and increase of conductivity.

The conductivity of all samples is actually increased after exposure to hydrogen atmosphere; the highest conductivity value was found in sample DST8, decreasing to about half in DST3 and DST5 and by one order of magnitude in DST10 at 650 °C. By XRD measurement, repeated after the reduction it is observed that DST10 degraded after reduction. Results are reported in Figure 7, together with the patterns obtained after sintering in air and discussed above. It is clear that XRD patterns of DST3 and DST5 overlap with each other, only showing the presence of a small quantity of TiO_2.

On the contrary, in the other two samples DST8 and DST10 after reduction additional phases were also found, that are Ti-Sr mixed oxides with different stoichiometry. This phenomenon is less prominent in DST8 and it doesn't affect the conductivity, while DST10 was strongly degraded and its conductivity decreased strongly.

In light of these results, the most promising candidate for use as anodic material in SOFC is the composition $Dy_{0.08}Sr_{0.92}TiO_3$ due to its sufficient chemical stability both under reducing and oxidizing conditions, coupled with highest conductivity and lowest activation energy within the series of samples. A direct comparison with the conductivity values reported in literature for other doped strontium titanate would be misleading because no optimization was carried out on the sintering protocol to maximize density and conductivity itself. Therefore, data reported in this work are helpful in selecting the most appropriate (promising) composition for further development as anodic SOFC material.

To get information about performance and stability of DST8 in operative conditions, a test in a complete solid oxide fuel cell, with standard materials for cathode and electrolyte, is needed. This topic will be the object of a following paper.

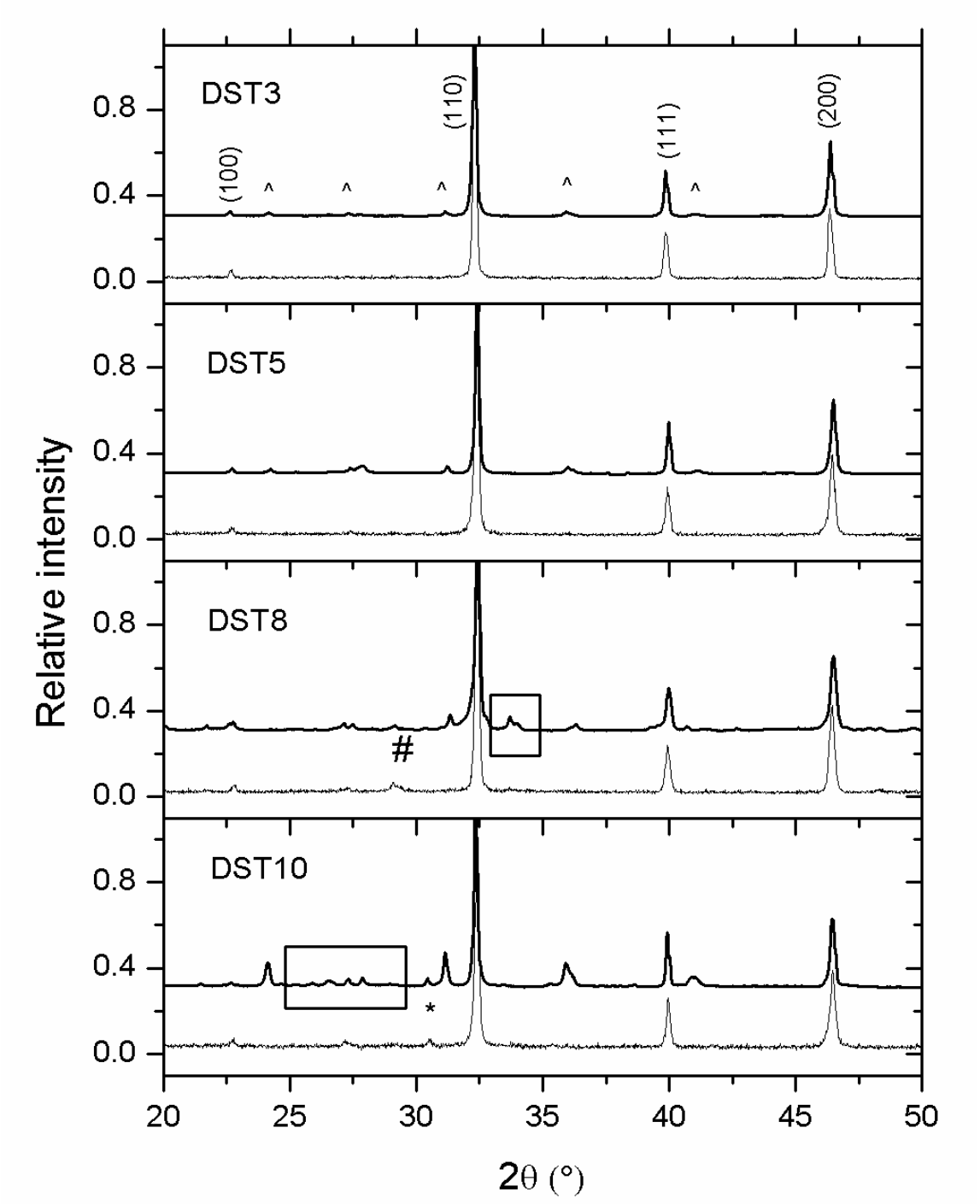

Figure 7. Comparison of XRD patterns obtained before (thin line) and after reduction (thick line). Miller indexes of $SrTiO_3$ are also reported with major reflections of TiO_2 (^), Dy_2O_3 (#) and $Dy_2Ti_2O_7$ (*) secondary phases. Peaks of mixed Ti, Sr oxides, different from $SrTiO_3$ are highlighted by rectangles

4. Conclusion

In the present work, Dy-doped $SrTiO_3$ system was studied for the first time as candidate for anodic materials. Microstrain, crystallite size and density decreased with increasing of Dy content for $x \leq 0.08$, where a minimum was detected for all quantities, and then increased again for $x = 0.10$. Moreover, samples with $x \leq 0.05$ are single phase, while for $x \geq 0.08$ about 6 wt.% of secondary phases are formed. In air, the conductivity is predominantly mixed ionic-electronic type for $x \leq 0.05$, becoming ionic for $x \geq 0.08$. It is observed that conductivity, for all composition, increased passing from air to hydrogen and activation energy decreased. $Dy_{0.05}Sr_{0.95}TiO_{3-\delta}$ shows the highest conductivity in air whereas $Dy_{0.08}Sr_{0.92}TiO_{3-\delta}$ in H_2 atmosphere. Results can be explained by considering different incorporation mechanisms, for different amounts of Dy, particularly simultaneous incorporation at Sr- and Ti-sites, incorporation at Ti-site with oxygen vacancies compensation or incorporation at Sr-site with electron compensation. Some degradation is observed by XRD for $x \geq 0.08$ after reduction, that increases by increasing Dy content, being still limited in DST8 and not affecting conductivity. Hence, DST8 may be considered as a promising anode material for solid oxide fuel cells. In the future, it will be tested in operative SOFC conditions to check performances. Moreover, aging tests will be performed, to check the effective stability.

References:

1. S. C. Singhal, Advances in solid oxide fuel cell technology. Solid State Ion. 135 (2000) 305-313.
2. K. Joon, Fuel cells – a 21st century power system J. Power Sources. 71 (1998) 12-18.
3. N. Q. Minh, Ceramic Fuel Cells. J. Am. Ceram. Soc. 76 (1993) 563-588.
4. B C. H. Steele, A. Heinzel. Materials for fuel-cell technologies. Materials for Sustainable Energy, (2010) 224-231.
5. Choudhury, A.; Chandra, H.; Arora, A., Application of solid oxide fuel cell technology for power generation—A review. Renewable and Sustainable Energy Reviews. 20 (2013) 430-442.
6. Andersson, M.; Sundèn, B., Technology review – Solid Oxide Fuel Cell. Report 2017:359. Publisher: Energiforsk, 2017; ISBN 978-91-7673-359-2. Available on line: https://energiforskmedia.blob.core.windows.net/media/22411/technology-review-solid-oxide-fuel-cell-energiforskrapport-2017-359.pdf .
7. F. S. Silva, T. M. Souza, Novel materials for solid oxide fuel cell technologies: A literature review, International Journal of Hydrogen Energy. 42 (2017) 26020-36.
8. Y. Leng, S. H. Chan, Q. Liu, Development of LSCF–GDC composite cathodes for low-temperature solid oxide fuelcells with thin film GDC electrolyte. Int. J. Hydrogen Energy 33 (2008) 3808-17.
9. C. L. Chu, J. Y. Wang, S. Lee, Effects of $La_{0.67}Sr_{0.33}MnO_3$ protective coating on SOFC interconnect by plasma-sputtering. Int. J. Hydrogen Energy 33 (2008) 2536-46.
10. Su, S.; Gao, X.; Zhang, Q.; Kong, W.; Chen, D., Anode- Versus Cathode-Supported Solid Oxide Fuel Cell: Effect of Cell Design on the Stack Performance. Int. J. Electrochem. Sci., 10, (2015), 2487 – 2503.
11. Krishnan, V. V. Recent developments in metal-supported solid oxide fuel cells. WIREs Energy Environ 2017, 6: null. doi: 10.1002/wene.246.

12. S. Presto, A. Barbucci, M. P. Carpanese, F. Han, R. Costa, M. Viviani. Application of La-Doped $SrTiO_3$ in Advanced Metal-Supported Solid Oxide Fuel Cells. Crystals 8(3) (2018) 134; doi:10.3390/cryst8030134.
13. Thorel, A. S.; Abreu, J.; Ansar, S.-A.; Barbucci, A.; Brylewski, T.; Chesnaud, A.; Ilhan, Z.; Piccardo, P.; Prazuch, J.; Presto, S.; Przybylski, K.; Soysal, D.; Stoynov, Z.; Viviani, M.; Vladikova D. Proof of concept for the dual membrane cell I. Fabrication and electrochemical testing of first prototypes. Journal of The Electrochemical Society, 2013, 160(4), F360-F366.
14. Presto, S.; Barbucci, A.; Viviani, M.; Ilhan, Z.; Ansar, S.-A.; Soysal, D.; Thorel, A. S.; Abreu, J.; Chesnaud, A.; Politova, T.; Przybylski, K.; Prazuch, J.; Brylewski, T.; Zhao, Z.; Vladikova, D.; Stoynov Z. IDEAL-Cell, innovative dual membrane fuel-cell: fabrication and electrochemical testing of first prototypes. ECS Transactions, 2009, 25 (2), 773-782.
15. Xu, J. ; Zhou, X.; Cheng, J.; Pan, L.; Wu; M.; Dong, X.; Sun, K. Electrochemical performance of highly active ceramic symmetrical electrode La0.3Sr0.7Ti0.3Fe0.7O3-δ-CeO2 for reversible solid oxide cells. Electrochimica Acta, 257 (2017) 64-72.
16. Matsuzaki, Y.; Yasuda, I. The poisoning effect of sulfur-containing impurity gas on a SOFC anode: Part I. Dependence on temperature, time, and impurity concentration. Solid State Ionics, 132 (2000) 261-269.
17. Khan, M. S.; Lee, S.-B.; Song, R.-H.; Lee, J.-W.; Lima, T.-H.; Park, S.-J. Fundamental mechanisms involved in the degradation of nickel–yttria stabilized zirconia (Ni–YSZ) anode during solid oxide fuel cells operation: A review. Ceramics International, 2016, 42, 35–48.
18. A. Atkinson, S. Barnett, R. J. Gorte, J. T. S. Irvine, A. J. McEvoy, M. Mogensen, et al. Advanced anodes for high-temperature fuel cells. Nat. Mater 3 (2004) 17-27.
19. S. W. Tao, J. T. S. Irvine, Discovery and characterization of novel oxide anodes for solid oxide fuel cells. Chem. Rec. 4 (2004) 83-95.

20. Slater, P.R.; Fagg, D.P.; Irvine, J.T.S. Synthesis and electrical characterization of doped perovskite titanates as potential anode materials for solid oxide fuel cells. Journal of Material Chemistry, 7 (1997) 2495-2498.
21. D. Neagu and J.T.S. Irvine. Structure and Properties of $La_{0.4}Sr_{0.4}TiO_3$ Ceramics for Use as Anode Materials in Solid Oxide Fuel Cells. Chem. Mater. 22 (2010) 5042-5053.
22. C. Perillat-Merceroz, G. Gauthier, P. Roussel, M. Huve, P. Gelin, R-N Vannier. Synthesis and Study of a Ce-Doped La/Sr Titanate for Solid Oxide Fuel Cell Anode Operating Directly on Methane. Chem. Mater. 23 (2011) 1539–1550.
23. O. A. Marina, N. L. Canfield, J. W. Stevenson, Thermal, electrical, and electrocatalytical properties of lanthanum-doped strontium titanate. Solid State Ion. 149 (2002) 21-28.
24. Savaniu, C.; Irvine, J.T.S. Reduction studies and evaluation of surface modified A-site deficient La-doped SrTiO3 as anode material for IT-SOFCs. Journal of Material Chemistry, 2009, 19, 8119-8128.
25. X. Shen, T. Kawabata, K. Sasaki. Redox-stable $Sr_{0.9}La_{0.1}TiO_3$-supported SOFC single cells. International journal of hydrogen energy. 42 (2017) 6941-6949.
26. A Flores JJ, et al. Advances in the development of titanates for anodes in SOFC. International Journal of Hydrogen Energy. (2018), https://doi.org/10.1016/j.ijhydene.2018.05.171
27. Hui, S.; Petric, A. Evaluation of yttrium-doped SrTiO3 as an anode for solid oxide fuel cells. Journal of European Ceramic Society, 2002, 22, 1673-1681.
28. Hui, S.; Petric, A. Electrical Properties of Yttrium-Doped Strontium Titanate under Reducing Conditions. Journal of the Electrochemical Society, 2002, 149(1), J1-10.
29. Hui, S.; Petric, A. Electrical conductivity of yttrium-doped SrTiO3: influence of transition metal additives. Material Research Bulletin, 2002, 37(7), 1215-1231.

30. S. Singh, P. A. Jha, S. Presto, M. Viviani, A.S.K. Sinha, S. Varma, P. Singh. Structural and electrical conduction behaviour of yttrium doped strontium titanate: anode material for SOFC application. Journal of Alloys and Compounds. 748 (2018) 637-644.
31. Panahi, S.N., Samadi, H. & Nemati, A. Effect of Samarium Oxide on the Electrical Conductivity of Plasma-Sprayed SOFC Anodes. JOM 68 (2016) 2569-2573.
32. A.A. Yaremchenko, S.G. Patrício, J.R. Frade. Thermochemical behavior and transport properties of Pr-substituted $SrTiO_3$ as potential solid oxide fuel cell anode. Journal of Power Sources. 245 (2014) 557-569.
33. A. M. Hussain, J. V. T. Høgh, T. Jacobsen, N. Bonanos. Nickel-ceria infiltrated Nb-doped $SrTiO_3$ for low temperature SOFC anodes and analysis on gas diffusion impedance. International journal of hydrogen energy. 37 (2012) 4309-4318.
34. T.D. McColm, J.T.S. lrvine. B Site Doped Strontium Titanate as a Potential SOFC Substrate. lonics 7 (2001) 116-121.
35. D. N. Miller, J. T. S. Irvine. B-site doping of lanthanum strontium titanate for solid oxide fuel cell anodes. Journal of Power Sources. 196 (2011) 7323–7327.
36. J. Li, T. Lv, N. Hou, P. Li, X. Yao, L. Fan, T. Gan, Y. Zhao, Y. Li. Molybdenum substitution at the B-site of lanthanum strontium titanate anodes for solid oxide fuel cells. International journal of hydrogen energy. 42 (2017) 22294-22301.
37. H. Yoon, J. Zou, N. M. Sammes, J. Chung. Ru-doped lanthanum strontium titanates for the anode of solid oxide fuel cells. International journal of hydrogen energy. 40 (2015) 10985-10993.
38. A. Yaqub, N. K. Janjua, C. Savaniu, John T.S. Irvine. Synthesis and characterization of B-site doped $La_{0.20}Sr_{0.25}Ca_{0.45}TiO_3$ as SOFC anode materials. International journal of hydrogen energy. 40 (2015) 760-766.

39. F. Napolitano, D.G. Lamas, A. Soldati, A. Serquis. Synthesis and structural characterization of Co-doped lanthanum strontium titanates. International journal of hydrogen energy. 37 (2012) 18302-18309.
40. Blennow, P.; Sudireddy, B. R.; Persson, Å.H.; Klemensø, T.; Nielsen, J.; Thydén, K. Infiltrated SrTiO3:FeCr-based Anodes for Metal-Supported SOFC. Fuel Cells, 2013, 13, 494–505.
41. Qi-Guo Hu, Zong-Yang Shen, Yue-Ming Li, Zhu-Mei Wang, Wen-Qin Luo, Zhi-Xiang Xie, Enhanced energy storage properties of dysprosium doped strontium titanate ceramics, Ceramics International 40 (2014) 2529–2534.
42. Zong–Yang Shen & Yue–Ming Li & Qi–Guo Hu & Wen–Qin Luo & Zhu–Mei Wang Dielectric properties of B–site charge balanced Dy–doped SrTiO3 ceramics for energy storage. J Electroceram (2015) 34:236–240.
43. David R. Lide, ed., CRC Handbook of Chemistry and Physics, 89th Edition (Internet Version 2009), CRC Press/Taylor and Francis, Boca Raton, FL
44. K. Singh, J. Nowotny, V. Thangadurai, Amphoteric oxide semiconductors for energy conversion devices: a tutorial review. Chem. Soc. Rev., 42 (2013) 1961-1972. doi: 10.1039/c2cs35393h
45. K. Uematsu, O. Sakurai, N. Mizutani, M. Kato, Electrical properties of La-doped SrTiO3 (La: 0.1 to 2.0 at %) single crystals grown by xenon-arc image floating zone method. J. Mater. Sci. 19 (1984) 3671-3679.
46. J. Liu, C.L. Wang, H. Peng, W.B. Su, H.C. Wang, J.C. Li, J.L. Zhang, L.M. Mei Thermoelectric Properties of Dy-Doped SrTiO3 Ceramics , Journal of Electronic Materials, 41(11) (2012) 3073–3076.
47. G.K. Williamson, W.H. Hall, X-ray line broadening from filed aluminium and wolfram. Acta Metall. 1 (1953) 22–31.

48. P. Kumar, S. Presto, A.S.K. Sinha, S. Varma, M. Viviani, P. Singh, Effect of samarium (Sm^{3+}) doping on structure and electrical conductivity of double perovskite Sr2NiMoO6 as anode material for SOFC Journal of Alloys and Compounds. 725, (2017) 1123-1129.
49. P. Wynblatt, G.S. Rohrer, F. Papillon, Grain boundary segregation in oxide ceramics, J. Eur. Ceram. Soc., 23 (2003), pp. 2841-2848.
50. N. Bonanos, B.C.H. Steele, E.P. Butler, in Impedance Spectroscopy Theory, Experiment, and Applications, ed. E. Barsoukov, J. Ross Macdonald, John Wiley & Sons, New Jersey, Second Edition, 2005, chapter 4, pp. 219,
51. Mollerup, P. L., Bonanos, N., Holtappels, P., & Tullmar, P. B. (2013). New Electrolytes for CO2 Electrolysis Cells. Kgs. Lyngby: Department of Energy Conversion and Storage, Technical University of Denmark. PhD Thesis
52. Knauth P, Tuller HL. Solid-State Ionics: Roots, Status, and Future Prospects. J Am Ceram Soc. 85 (2004) 1654–80. doi:10.1111/j.1151-2916.2002.tb00334.x,
53. Xie S, Liu W, Wu K, Yang PH, Meng GY, Chen CS. Mixed oxygen ionic and electronic conduction in $CaFe_{0.2}Ti_{0.8}O_{3-\delta}$: a combined oxygen permeation and electrical conductivity study. Solid State Ionics. 118 (1999) 23–8. doi:10.1016/S0167-2738(98)00453-6
54. M.T. Buscaglia, M. Viviani, V. Buscaglia, C. Bottino, P. Nanni, Incorporation of Er^{3+} into BaTiO3, J. Am. Ceram. Soc. 85 (2002) 1569–1575. doi:10.1111/j.1151-2916.2002.tb00313.x.